

## Rapid fore-arc extension and detachment-mode spreading following subduction initiation

Maffione, Marco; Morris, Antony; Anderson, Mark; Omer, Ahmed; van Hinsbergen, Douwe

DOI:

[10.1016/j.epsl.2017.08.040](https://doi.org/10.1016/j.epsl.2017.08.040)

License:

Creative Commons: Attribution-NonCommercial-NoDerivs (CC BY-NC-ND)

*Document Version*

Peer reviewed version

*Citation for published version (Harvard):*

Maffione, M, Morris, A, Anderson, M, Omer, A & van Hinsbergen, D 2017, 'Rapid fore-arc extension and detachment-mode spreading following subduction initiation', *Earth and Planetary Science Letters*, vol. 748, pp. 76-88. <https://doi.org/10.1016/j.epsl.2017.08.040>

[Link to publication on Research at Birmingham portal](#)

**Publisher Rights Statement:**

published on <https://doi.org/10.1016/j.epsl.2017.08.040>

**General rights**

Unless a licence is specified above, all rights (including copyright and moral rights) in this document are retained by the authors and/or the copyright holders. The express permission of the copyright holder must be obtained for any use of this material other than for purposes permitted by law.

- Users may freely distribute the URL that is used to identify this publication.
- Users may download and/or print one copy of the publication from the University of Birmingham research portal for the purpose of private study or non-commercial research.
- User may use extracts from the document in line with the concept of 'fair dealing' under the Copyright, Designs and Patents Act 1988 (?)
- Users may not further distribute the material nor use it for the purposes of commercial gain.

Where a licence is displayed above, please note the terms and conditions of the licence govern your use of this document.

When citing, please reference the published version.

**Take down policy**

While the University of Birmingham exercises care and attention in making items available there are rare occasions when an item has been uploaded in error or has been deemed to be commercially or otherwise sensitive.

If you believe that this is the case for this document, please contact [UBIRA@lists.bham.ac.uk](mailto:UBIRA@lists.bham.ac.uk) providing details and we will remove access to the work immediately and investigate.

1 **Rapid fore-arc extension and detachment-mode spreading**  
2 **following subduction initiation**

3

4 Antony Morris<sup>a\*</sup>, Mark W. Anderson<sup>a</sup>, Ahmed Omer<sup>a,#</sup>, Marco Maffione<sup>b</sup>,  
5 Douwe J. J. van Hinsbergen<sup>c</sup>

6

7 <sup>a</sup> *School of Geography, Earth and Environmental Sciences, University of Plymouth,*  
8 *Drake Circus, Plymouth PL4 8AA, UK*

9 <sup>b</sup> *School of Geography, Earth and Environmental Sciences, University of*  
10 *Birmingham, Edgbaston, Birmingham B15 2TT, UK*

11 <sup>c</sup> *Department of Earth Sciences, University of Utrecht, Utrecht, Netherlands*

12

13 \* Corresponding author.

14 *E-mail address: [amorris@plymouth.ac.uk](mailto:amorris@plymouth.ac.uk) (A. Morris).*

15

16

17 **ABSTRACT**

18

19 Most ophiolites have geochemical signatures that indicate formation by  
20 suprasubduction seafloor spreading above newly initiated subduction zones, and  
21 hence they record fore-arc processes operating following subduction initiation. They  
22 are frequently underlain by a metamorphic sole formed at the top of the downgoing  
23 plate and accreted below the overlying suprasubduction zone lithosphere

---

# Permanent address: Technical Institute of Kirkuk, Kirkuk, Republic of Iraq

24 immediately following ophiolite formation. Paleomagnetic analyses of ophiolites can  
25 provide important insights into the enigmatic geodynamic processes operating in this  
26 setting via identification of tectonic rotations related to upper plate extension. Here  
27 we present net tectonic rotation results from the Late Cretaceous Mersin ophiolite of  
28 southern Turkey that document rapid and progressive rotation of ophiolitic rocks and  
29 their associated metamorphic sole. Specifically, we demonstrate that lower crustal  
30 cumulate rocks and early dykes intruded into the underlying mantle section have  
31 undergone extreme rotation around ridge-parallel, shallowly-plunging axes,  
32 consistent with oceanic detachment faulting during spreading. Importantly, later  
33 dykes cutting the metamorphic sole experienced rotation around the same axis but  
34 with a lower magnitude. We show that these rotations occurred via a common  
35 mechanism in a pre-obduction, fore-arc setting, and are best explained by combining  
36 (hyper)extension resulting from detachment-mode, amagmatic suprasubduction zone  
37 spreading in a fore-arc environment with a recently proposed mechanism for  
38 exhumation of metamorphic soles driven by upper plate extension. Available age  
39 constraints demonstrate that extreme rotation of these units was accommodated  
40 rapidly by these processes over a time period of  $< \sim 3$  Myr, comparable with rates of  
41 rotation seen in oceanic core complexes in the modern oceans.

42

43 *Keywords:* ophiolite; paleomagnetism; subduction initiation; suprasubduction zone;  
44 fore-arc extension; metamorphic sole

45

46

47

48

## 49 **1. Introduction**

50

51 Ophiolites provide insights into fundamental oceanic tectonic processes associated  
52 with their formation at spreading axes and subsequent intraoceanic- and  
53 emplacement-related deformation. The majority of the world's ophiolites have a  
54 geochemical signature interpreted as indicating formation above newly initiated  
55 intraoceanic subduction zones, in so-called suprasubduction zone environments (e.g.  
56 Pearce and Robinson, 2010). This setting can also account for the observation that  
57 ophiolite accretion is often closely followed by subduction-related emplacement onto  
58 continental margins (Robertson 2002). In contrast to true mid-ocean ridge systems,  
59 suprasubduction zone ophiolite formation and subsequent evolution is the result of a  
60 complex process controlled by both the subducting plate and tectonic processes in  
61 the fore-arc region. This is clearly demonstrated by the occurrence of so-called  
62 metamorphic soles below many suprasubduction zone ophiolites. Metamorphic soles  
63 are thin (< 500 m) layers of granulite to greenschist facies rocks, which experienced  
64 high temperature and pressure metamorphism (850-900°C, 10-15 kbar) above a  
65 subducting lithosphere, prior to their accretion to the overriding plate (for a review  
66 see van Hinsbergen *et al.*, 2015). In several well-preserved ophiolites like that of  
67 Oman, the metamorphic sole is spread over a broad area below the ophiolite, up to c.  
68 100 km away from the paleo-trench, suggesting original accretion as a large semi-  
69 continuous metamorphic layer. The accretion of metamorphic soles below ophiolites  
70 necessarily requires some sort of fore-arc thinning to exhume the sole from peak  
71 metamorphic depths, either tectonically via extension of the overriding plate (e.g.  
72 Hacker and Gnos, 1997), or magmatically via partial melting and resulting volume  
73 decrease of the forearc mantle wedge below the newly formed suprasubduction zone

74 crust (van Hinsbergen *et al.*, 2015). The similarity of ages of ophiolitic crust and peak  
75 metamorphism of associated metamorphic soles observed in nearly all ophiolites  
76 indicates that spreading and metamorphic sole exhumation are almost simultaneous  
77 processes, and both occur during or shortly after subduction initiation.

78

79 Obtaining geological evidence that constrains the kinematics and timing of tectonic  
80 processes affecting fore-arc systems during subduction initiation in the modern  
81 oceans is difficult as incipient subduction zones are rare (Gurnis *et al.*, 2004). Hence,  
82 well-exposed ophiolites provide important records of fore-arc processes operating  
83 during and following subduction initiation that are otherwise difficult to investigate  
84 (Stern and Bloomer, 1992; Robertson 2002). Numerous studies have highlighted how  
85 paleomagnetic analyses of ophiolites can help to unravel the tectonic evolution of  
86 these systems. A focus has been the Tethyan ophiolites of the eastern  
87 Mediterranean/Middle East region, where magnetic techniques have been used to  
88 constrain the structure and orientation of suprasubduction spreading axes (e.g.  
89 Allerton and Vine, 1987; Hurst *et al.*, 1992; Morris and Maffione, 2016; Maffione *et*  
90 *al.*, 2017), patterns of magmatic flow during crustal accretion (e.g. Staudigel *et al.*,  
91 1992; Granot *et al.*, 2011), the kinematics of transform fault systems (e.g. Morris *et*  
92 *al.*, 1990; MacLeod *et al.*, 1990; Morris and Maffione, 2016), and the response of the  
93 upper plate to impingement of continental margins with subduction zones (Clube *et*  
94 *al.*, 1985; Inwood *et al.*, 2009; Morris *et al.*, 2002).

95

96 Renewed interest in ophiolites has followed the discovery of the importance of  
97 oceanic detachment faulting and the formation of oceanic core complexes (OCCs) in  
98 slow-ultraslow spreading lithosphere in the Atlantic and Indian Oceans (e.g. Smith *et*

99 *al.*, 2008; MacLeod *et al.*, 2017) and the definition of a new amagmatic “detachment-  
100 mode” of seafloor spreading (Escartín and Canales 2011). This is fundamentally  
101 different from classic magmatic spreading and involves plate divergence being taken  
102 up by slip on lithospheric-scale faults that rotate during displacement, resulting in  
103 exhumation of their footwall sections and exposure of lower crustal and mantle rocks  
104 on the seafloor. Studies of samples recovered by scientific ocean drilling have shown  
105 45-65° rolling-hinge rotations of OCC footwalls in the Atlantic Ocean around ridge-  
106 parallel, sub-horizontal axes (Garcés and Gee, 2007; Morris *et al.*, 2009; MacLeod *et*  
107 *al.*, 2011). This characteristic has allowed Maffione *et al.* (2013) to extend the record  
108 of detachment-mode spreading back to the Jurassic by demonstrating the existence  
109 of a fossil OCC preserved within the Mirdita ophiolite of Albania. More recently,  
110 Maffione *et al.* (2015) showed that oceanic detachment faulting was responsible for  
111 large tectonic rotations and extensional thinning of fore-arc lithosphere preserved in  
112 the Cretaceous ophiolites of southern Tibet. This led them to propose a new concept  
113 of “fore-arc hyperextension”, demonstrating how the exchange of ideas between  
114 studies in the modern oceans and in ophiolites can lead to advances in our  
115 understanding of lithospheric processes.

116

117 Here we present the first paleomagnetic data from the Late Cretaceous Mersin  
118 ophiolite of southern Turkey. Like many Tauride ophiolites (Dilek *et al.*, 1999), Mersin  
119 consists predominantly of tectonized mantle rocks and ultramafic/mafic cumulates,  
120 with no sheeted dyke complex and only limited exposures of extrusive rocks, and is  
121 underlain by a metamorphic sole that has  $^{40}\text{Ar}$ - $^{39}\text{Ar}$  cooling ages that are similar to  
122 the age of the ophiolitic magmatic rocks (Parlak *et al.*, 2013; van Hinsbergen *et al.*,  
123 2016). Our data constrain the axes, magnitudes and timing of tectonic rotations in

124 these units, and provide evidence for rapid fore-arc (hyper)extension via detachment-  
125 mode seafloor spreading (Escartin and Canales, 2011). We show that this style of  
126 Neotethyan suprasubduction zone spreading provides a viable mechanism to explain  
127 the exhumation of metamorphic soles, their structural disruption following welding to  
128 the base of the lithosphere, and the lack of upper crustal sequences in many Tauride  
129 ophiolites.

130

## 131 **2. The Mersin ophiolite**

132

133 The Mersin ophiolite complex outcrops over a 60 km long, 25 km wide area in  
134 southern Turkey (Fig. 1a). It consists of an Upper Cretaceous ophiolite sequence,  
135 underlain by metamorphic sole rocks and then by the Mersin Mélange (Fig. 1b;  
136 Parlak and Delaloye, 1996, 1999; Parlak *et al.*, 2013). These units form the highest  
137 structural unit of the uppermost Cretaceous-Eocene Tauride fold-thrust belt  
138 dominated by Paleozoic-Mesozoic platform carbonates (Robertson, 2002).

139

140 The ophiolite has a suprasubduction zone geochemical signature (Parlak *et al.*,  
141 1996a) and consists of tectonized peridotites (harzburgites and dunites), ultramafic  
142 and mafic cumulates, isotropic gabbro, minor plagiogranites, and rare basalts  
143 associated with deep marine sediments (Parlak *et al.*, 1996a). The cumulate rocks  
144 are best exposed along the Sorgun valley (between the villages of Sorgun and  
145 Arsalanlı; Fig. 1a), where ~800 m of ultramafic cumulates at the base pass upwards  
146 into ~2500 m of modally layered gabbroic rocks consisting of gabbro, olivine gabbro  
147 and anorthosite (Parlak *et al.*, 1996a). Way-up criteria (mineralogical grading;  
148 evidence of scouring at the base of some layers; Fig. 2) indicate that steeply-dipping

149 modal compositional layering in the gabbros is in places overturned. The cumulate  
150 layers are occasionally intruded at a high angle by thin, fine-grained basaltic dykes.  
151

152 Lower levels of the ophiolite are best exposed in the Fındıklı valley area (Fig.  
153 1a), nearly 20 km to the NE of the Sorgun valley, providing sections through both the  
154 mantle sequence and the metamorphic sole. The latter has a thickness of about 50-  
155 70 m and consists predominantly of amphibolites, amphibolitic schists, epidote-  
156 amphibolite schists, quartz-mica schists, calcschists and marble, with a typical  
157 inverted metamorphic zonation from upper amphibolite at the top to greenschist  
158 facies at the bottom (Parlak *et al.*, 1996b). The sole rocks are intensely deformed,  
159 with development of a pronounced foliation, a NW-SE-trending mineral stretching  
160 lineation and intrafolial folds (Parlak *et al.*, 1996b). Kinematic indicators all indicate a  
161 top to the NW shear sense during formation of the sole (Parlak *et al.*, 1996b).

162

163 Both the tectonized harzburgite and sole are cut by undeformed, discrete doleritic  
164 dykes composed of plagioclase, clinopyroxene and amphibole, with subophitic and  
165 microgranular textures and variable degrees of hydrothermal alteration. They have  
166 geochemical signatures similar to evolved island-arc tholeiites and were derived from  
167 a mantle wedge that underwent previous melt extraction and subsequent  
168 metasomatism by LILE- and light REE-enriched fluids (Dilek *et al.*, 1999). Dykes  
169 hosted by tectonized harzburgite are up to 5 m thick and dip at ~30° to the ~ESE,  
170 whereas those hosted by the metamorphic sole are characteristically thinner (< 1 m),  
171 clearly post-metamorphic and post-shearing, and dip at ~55° to the ~NW.

172



173 Available high precision  $^{40}\text{Ar}$ – $^{39}\text{Ar}$  and U-Pb age constraints for the Mersin ophiolite  
174 and its metamorphic sole are summarized in Table 1. Only one U-Pb zircon date is  
175 available from the Mersin gabbros (Parlak et al., 2013), yielding an age of  $82.8\pm 4.0$   
176 Ma. This is deemed unreliable, however, due to evidence for hydrothermal alteration  
177 of the dated zircons, and the age of crystallization of the suprasubduction zone crust  
178 regionally is considered by Parlak et al. (2013) to be  $\sim 89$  Ma. The remaining data  
179 indicate that intrusion of dykes into the mantle sequence, formation of the  
180 metamorphic sole (cooling through amphibolite facies conditions) and intrusion of  
181 dykes through the sole were broadly synchronous events. This has important  
182 implications for the rapidity of the rotations determined from the paleomagnetic data  
183 presented here.

184

### 185 **3. Sampling and methods**

186

187 To quantify tectonic rotations that have affected the Mersin ophiolite, we sampled the  
188 lower crustal sequence (ultramafic and gabbroic cumulates) exposed continuously  
189 along the Sorgun valley section (Fig. 1a), together with dolerite dykes cutting  
190 tectonized harzburgites of the mantle sequence, and dolerite dykes cutting the  
191 metamorphic sole of the ophiolite (both exposed near the village of Fındıklı; Fig  
192 1a). An average of eight samples per site were drilled *in situ* using standard  
193 paleomagnetic procedures, yielding up to 13 specimens per site for analysis.  
194 Sampling was restricted to exposures that showed either consistent planar layering in  
195 cumulate rocks or dykes with parallel planar margins. Structural orientations were  
196 measured in the field to an accuracy of  $\pm 5^\circ$ .

197

198 Natural remanences were measured in the University of Plymouth palaeomagnetic  
199 laboratory using either Molspin or AGICO JR-6A fluxgate spinner magnetometers  
200 (with respective noise levels of  $0.05 \times 10^{-3}$  and  $0.01 \times 10^{-3}$  A/m). Specimens were  
201 subjected to either alternating field (AF) demagnetization using an AGICO LDA-3A  
202 demagnetizer in 13 incremental steps from 5 to 100 mT or thermal demagnetization  
203 using a Magnetic Measurements MMTD80A demagnetizer with 19 temperature  
204 increments from 100 to 580°C (or until complete demagnetization). Demagnetization  
205 data were displayed on orthogonal vector plots and remanence components isolated  
206 via principal component analysis using MacPaleomag software (written by Jeff Gee,  
207 Scripps Institution of Oceanography). Site mean directions were evaluated using  
208 Fisherian statistics on virtual geomagnetic poles (VGPs) corresponding to the  
209 isolated characteristic remanent magnetizations (ChRMs). Paleomagnetic quality  
210 criteria proposed by Deenen et al. (2011) were adopted to estimate the reliability of  
211 the ChRM/VGP distribution at the site level. In particular, the VGP scatter (i.e.,  $A_{95}$ )  
212 obtained at each site was compared to the expected scatter induced by paleosecular  
213 variation (PSV) of the geomagnetic field (i.e.,  $A_{95min} - A_{95max}$ ) to assess whether PSV  
214 was sufficiently represented in our datasets (Deenen *et al.*, 2011). For values of  $A_{95} <$   
215  $A_{95min}$  PSV is not adequately represented, indicating insufficient time averaging of the  
216 geomagnetic field (i.e. resulting from rapid cooling), slow cooling and protracted  
217 acquisition of remanence (such that PSV is largely averaged at the specimen level)  
218 or remagnetization. Conversely, values of  $A_{95} > A_{95max}$  may indicate additional  
219 (tectonic) processes responsible for an enhanced scatter of paleomagnetic  
220 directions. Site mean magnetization directions were interpreted using a net tectonic  
221 rotation approach (Allerton and Vine, 1987; Morris *et al.*, 1998) to determine rotation

222 axes and magnitudes and recover the initial strikes of dykes. This technique is  
223 discussed more fully below.

224

225 Rock magnetic experiments were performed to characterize remanence-carrying  
226 minerals in sampled lithologies. The high-temperature (20-700°C) variation of  
227 magnetic susceptibility,  $k$ , of representative samples was measured in an argon  
228 atmosphere using an AGICO Kappabridge KLY-3S coupled with a CS-3 furnace.  
229 Curie temperatures were determined from these experiments by the Petrovsky &  
230 Kapička (2006) method on  $1/k$  data using the AGICO program Cureval v. 8.0.2.  
231 Isothermal remanent magnetization (IRM) acquisition experiments were conducted  
232 on representative samples to determine coercivity spectra (using a Molspin pulse  
233 magnetizer to apply peak fields up to 800 mT, with resulting IRMs measured using an  
234 AGICO JR-6A spinner magnetometer), followed by backfield IRM experiments to  
235 determine coercivities of remanence. Ferromagnetic phases were further  
236 characterized in thin section by optical microscopy and by EDX spectral analyses  
237 performed on a JEOL7001 FEG-SEM and analyzed using Oxford Instruments Aztec  
238 software.

239

## 240 **4. Results and analysis**

241

### 242 *4.1 Magnetic mineralogy and palaeomagnetic results from the ophiolite*

243

244 High-temperature variation of magnetic susceptibility experiments revealed  
245 consistent maximum Curie temperatures of ~580°C (Figure 3a), indicating that the  
246 ferromagnetic fraction in both cumulate rocks and dykes includes near-stoichiometric

247 magnetite. Some specimens exhibit increased susceptibility upon cooling, suggesting  
248 production of new magnetite during heating. A limited number of specimens (e.g.  
249 specimen MC1804 in Fig. 3a) show a hump in the heating curve between 150-400°C.  
250 The increasing temperature limbs of these humps are reversible until 300°C, but  
251 become irreversible after further heating, suggesting the presence of  
252 titanomagnetite/titanomaghemite in addition to magnetite. IRM acquisition  
253 experiments show that saturation is reached at applied fields of 200-300 mT (Figure  
254 3b) indicating presence of low coercivity minerals in these rocks. Backfield IRM  
255 experiments yield coercivity of remanence values of 24-53 mT suggesting presence  
256 of fine-grained single domain or pseudo-single domain magnetite. These rock  
257 magnetic observations are consistent with petrographic and SEM analyses that show  
258 that magnetite and minor titanomagnetite are the dominant oxides present in both  
259 cumulate rocks and dykes. In the ultramafic cumulates (sites MC01-03), secondary  
260 magnetite is present in serpentinized olivine grains, whereas primary magnetite (plus  
261 titanomagnetite) with little alteration is observed in the cumulate gabbros and diabase  
262 dykes. Ferromagnetic pyrrhotite is also occasionally seen in the dykes, but  
263 demonstrably carries the same magnetization direction as the dominant magnetite  
264 phase. Overall, these results are entirely compatible with those obtained in other Late  
265 Cretaceous Neotethyan ophiolites in this region (e.g. Troodos, Hatay, Baër-Bassit,  
266 Alihoca, Göksun, Divriği; Morris *et al.*, 1998, 2002; Inwood *et al.*, 2009; Morris and  
267 Maffione, 2016; Maffione *et al.*, 2017), where magnetic remanences have been  
268 shown to be of primary, pre-deformational origin, acquired during or shortly after  
269 seafloor spreading.  
270

271 Intensities of natural remanences in these rocks vary by lithology, with highest  
272 average intensities in the layered gabbros (1.12 A/m) and lower values of 132 mA/m  
273 and 80 mA/m in the ultramafic cumulates and dykes, respectively. Stable  
274 components of magnetization were isolated at all sites, following removal of  
275 occasional minor secondary components during initial demagnetization. Typical  
276 examples of demagnetization behaviour are shown in Fig. 4. Most samples are  
277 dominated by univectorial, single component decay to the origin. Both AF and  
278 thermal demagnetization experiments yielded identical remanence directions (Fig. 4).  
279 Stable components of magnetization were identified from individual specimens and  
280 subsequently combined to give a mean ChRM for each site. These *in situ* magnetic  
281 remanences are given in Table 2 and shown with corresponding specimen directions  
282 and VGPs in the stereographic equal area projections of Supplemental Fig. 1. With  
283 the exception of one specimen (at site MD11), all VGPs fell within the 45° cut-off at  
284 each site recommended by Johnson et al. (2008). Directions are unrelated to the  
285 present-day geocentric axial dipole field in the Mersin region ( $D = 000^\circ$ ,  $I = 56^\circ$ ),  
286 excluding recent remagnetization. Cumulate rocks (ultramafic cumulates and layered  
287 gabbros) have NE-directed *in situ* ChRMs with negative inclinations, indicating  
288 substantial tectonic rotation since magnetization acquisition. Dykes hosted in the  
289 mantle sequence also have *in situ* negative inclinations, whereas those cutting the  
290 metamorphic sole have shallow positive inclinations, with both sets having generally  
291 northerly declinations.

292

293 VGP scatter at 11 out of 28 sites (Table 2) is within the limits of that expected from  
294 PSV (Deenen *et al.*, 2011), consistent with a primary origin of the remanence.

295 Underrepresentation of PSV at remaining sites is interpreted to reflect significant

296 averaging of secular variation at the sample level during slow cooling of the cumulate  
297 rocks (as seen in samples of lower crustal gabbros recovered by scientific ocean  
298 drilling; Gee and Kent, 2007) and of dykes intruded into the mantle sequence and  
299 metamorphic sole.

300

#### 301 *4.2 Reference direction*

302

303 Remanence directions must be compared to an appropriate reference direction to  
304 determine the extent of tectonic rotation affecting the ophiolite. In our analysis, the  
305 reference direction has a declination =  $000^\circ$ , assuming an original normal magnetic  
306 polarity as the ophiolite formed during the Cretaceous Normal Superchron (C34N).  
307 This implies that calculated net rotations arise from a combination of plate motion  
308 and intra-plate deformation. The inclination of the reference direction was determined  
309 from paleolatitude estimates based on kinematic reconstructions (van Hinsbergen *et*  
310 *al.*, 2016) placed in the paleomagnetic reference frame of Torsvik *et al.* (2012).  
311 Uncertainties in the reference inclination relate to the reconstructed width of the  
312 Neotethys Ocean and the  $A_{95}$  error of the reference global apparent polar wander  
313 path. Reconstructions for the Late Cretaceous at 100-90 Ma constrain the  
314 Neotethyan spreading axis to lie between the southern margin of Eurasia at  $33\pm 3^\circ\text{N}$   
315 and the northern margin of Gondwana at  $16\pm 3^\circ\text{N}$ . We have no other paleolatitudinal  
316 control on the position of the future Mersin ophiolite within these limits, and therefore  
317 used a paleolatitude of  $24.5\pm 11.5^\circ\text{N}$  to encompass this range. Assuming a geocentric  
318 axial dipole field, this corresponds to a reference inclination of  $40.2\pm 15.4^\circ$ .

319

#### 320 *4.3 Determination of net tectonic rotations*

321

322 Standard paleomagnetic structural corrections involve untilting inferred  
323 paleohorizontal/vertical surfaces around strike-parallel axes. Corrected declinations  
324 are then compared to the reference direction to determine vertical axis rotations. This  
325 approach therefore arbitrarily decomposes the total deformation at a site into  
326 rotations around two orthogonal axes (vertical and horizontal). Interpretations then  
327 frequently focus entirely on the vertical axis rotations, ignoring the tilting component  
328 of the deformation. In complexly deformed terrains, where fold axes are seldom  
329 horizontal and where multiple phases of deformation may occur, this procedure can  
330 introduce serious declination errors (MacDonald, 1980). It is more appropriate,  
331 therefore, to describe the deformation at a site in terms of a single rotation about an  
332 inclined axis, which restores both the paleosurface to its initial orientation and the site  
333 mean magnetization vector to the reference direction. This single rotation may then  
334 be decomposed into any number of component rotations on the basis of additional  
335 structural data. Importantly, in the case of dykes, this approach can resolve rotations  
336 around margin-normal axes that are impossible to observe in the field and that act as  
337 a source of error when standard tilt corrections are employed (Morris and Anderson,  
338 2002). This approach also facilitates back-stripping of later rotations from the total  
339 deformation to recover earlier rotations.

340

341 Here we use the net tectonic rotation method of Allerton and Vine (1987), which has  
342 been employed effectively in numerous previous studies in ophiolites (e.g., Morris *et al.*,  
343 1990, 1998, 2002; Hurst *et al.*, 1992; Inwood *et al.*, 2009; Maffione *et al.*, 2015,  
344 2017; Morris and Maffione, 2016, van Hinsbergen *et al.*, 2016). This technique  
345 (Supplemental Fig. 2) can be applied to either paleovertical or paleohorizontal cases,

346 with the key assumption that no internal deformation of a sampled unit has occurred.  
347 In this case, the angle  $\beta$  between the site magnetization vector (SMV) and the  
348 present day pole to the paleosurface (PDP) remains constant during deformation  
349 (Allerton and Vine, 1987). A circle of radius  $\beta$  centred on the reference magnetization  
350 vector (RMV) therefore defines the locus of potential positions of the initial pole to the  
351 paleosurface. In the case of a dyke, the intersections of this circle with the horizontal  
352 represent the poles to two possible vertical initial dyke orientations (Supplemental  
353 Fig. 2), and additional constraints are required to select a preferred solution. If a  
354 vertical solution cannot be found then the dyke initial strike is invariable and fixed by  
355 the reference direction and we exclude the result from the analysis of restored dyke  
356 trends. In the case of cumulate rocks, an initial pole for the paleosurface is selected  
357 at the steepest point on the circle of radius  $\beta$  centred on the RMV in order to restore  
358 the structure to a minimum possible dip (Supplemental Fig. 2). In all cases, the SMV  
359 is then restored to the RMV and the PDP to its initial orientation by rotating around an  
360 axis at the intersection of the planes (great circles) bisecting the pairs of vectors  
361 (Supplemental Fig. 2). The net tectonic rotation is described by the azimuth and  
362 plunge of this rotation axis and the angle and sense of rotation.

363

364 In a modification of this method used here (Morris *et al.*, 1998; Koymans *et al.*, 2016),  
365 the effects of uncertainties on the input vectors are modelled by applying the Allerton  
366 and Vine (1987) algorithm to all combinations of three estimates of the reference  
367 inclination (mean plus two values at the edge of its error bar), and five estimates  
368 each of the SMV and present day pole to paleosurface (see Supplemental Fig. 2).  
369 This yields 75 estimates of the rotation parameters at each site, defining a non-  
370 circular distribution of acceptable rotation axes. The mean rotation axis can be



371 determined using Bingham statistics (orientation of maximum eigenvector), and the  
372 distribution of rotation angles plotted as histograms (Supplemental Fig. 2) and  
373 described by the mean value and standard deviation. Restored dyke trends can be  
374 represented on rose diagrams, with the mean strike determined from the  
375 intermediate eigenvector of the corresponding distribution of initial dyke poles. When  
376 distributions of rotation parameters at multiple sites overlap, these may be  
377 amalgamated to determine the most robust overall solution.

378

#### 379 *4.4 Net tectonic rotation solutions*

380

381 Out of 28 sampled sites, 25 gave net tectonic rotation solutions that are considered  
382 reliable. The three rejected sites are: (i) two dyke sites (MD01 and MD10) that gave  
383 scattered rotation axes and too few vertical solutions to be considered reliable; and  
384 (ii) a thin basaltic dyke (site MC10) intruding the layered gabbros of site MC09, that  
385 has a direction of magnetization statistically indistinguishable from its host rocks and  
386 that is not considered separately in the analysis of rotations. Mean net tectonic  
387 rotation parameters at the remaining sites are given in Table 3. In the case of the  
388 dyke sites (Table 3), our preferred solutions are those with NE-SW-directed rotation  
389 axes as these: (i) are consistent with results from the cumulate section; (ii) yield more  
390 consistent rotation angles between sites than the alternative solutions; and (iii)  
391 produce initial NE-SW dyke strikes that are in agreement with a regional-scale  
392 dataset of restored Neotethyan paleo-spreading directions recently reported by  
393 Maffione et al. (2017).

394

395 Fig. 5 illustrates the distributions of rotation parameters amalgamated by  
396 lithostratigraphic level in the ophiolite, whereas results at individual sites are shown in  
397 Supplemental Fig. 3 (for dyke sites) and Supplemental Fig. 4 (for cumulate sites).  
398 The analyses demonstrate that all levels of the Mersin ophiolite have experienced  
399 significant tectonic rotation around shallowly-plunging, NE-SW-directed axes. The  
400 overall mean rotation parameters (Tables 3 and 4; Fig. 5) for the three sampled  
401 lithostratigraphic levels are:

402

403 Cumulate section:  $120.0^{\circ} \pm 27.4^{\circ}$  clockwise rotation, axis =  $058^{\circ}/23^{\circ}$ , N = 1200

404 Mantle-hosted dykes:  $125.0^{\circ} \pm 8.4^{\circ}$  clockwise rotation, axis =  $047^{\circ}/-04^{\circ}$ , N = 257

405 Metamorphic sole-hosted dykes:  $45.0^{\circ} \pm 11.8^{\circ}$  clockwise rotation, axis =  $040^{\circ}/31^{\circ}$ , N =

406 290

407

408 where errors on rotation angles are  $\pm 1$  standard deviation.

409

410 This indicates that, despite a present day geographic separation of c. 20 km, the  
411 mantle and crustal sections of the ophiolite display structural integrity and  
412 experienced a common rotation history since acquiring their magnetizations. The  
413 metamorphic sole has also experienced rotation around a similar NE-SW-directed  
414 axis but with a much lower magnitude. This is considered to represent the latest  
415 phase of rotation to affect the ophiolite and potentially reflects a combination of  
416 intraoceanic and emplacement-related deformation. We assume that this net rotation  
417 also affected the overlying mantle and crustal sites. This assumption is supported by  
418 similar initial strikes for the mantle- and metamorphic sole-hosted dykes (Fig. 5), that  
419 suggests intrusion of these units occurred in a common stress field associated with

420 upper plate extension during formation of the ophiolite in a suprasubduction zone  
421 setting. The earlier phase of rotation affecting the mantle and crustal sections can  
422 then be determined by back-stripping the effect of the later rotation of the  
423 metamorphic sole prior to calculation of revised net tectonic rotation parameters for  
424 these units (Tables 3 and 4). This yields the following mean rotation parameters:

425

426 Cumulate section                     $79.9^{\circ} \pm 25.7^{\circ}$  clockwise rotation, axis =  $060^{\circ}/12^{\circ}$ , N = 1200

427 Mantle-hosted dykes:                 $92.4^{\circ} \pm 8.2^{\circ}$  clockwise rotation, axis =  $032^{\circ}/-15^{\circ}$ , N = 252

428 Combined:                               $82.1^{\circ} \pm 24.1^{\circ}$  clockwise rotation, axis  $056^{\circ}/08^{\circ}$ , N = 1452

429

430 The combined result represents the best estimate for early tilting of the sampled  
431 parts of the future ophiolite prior to emplacement of dykes into its metamorphic sole,  
432 and confirms that all phases of deformation involved rotation around similar, shallow  
433 NE-directed axes. Moreover, given the close timing of crustal accretion, cooling of  
434 the metamorphic sole and dyke intrusion (Parlak and Delaloye, 1996, 1999; Dillek et  
435 al., 1999; Parlak *et al.*, 2013), these data indicate that rotations accumulated  
436 progressively within the ophiolite over a very short time interval of  $< \sim 3$  Myr, requiring  
437 a tectonic environment capable of generating rapid and large rotations.

438

## 439 **5. Discussion**

440

### 441 *5.1 Tectonic environment for extreme and rapid early rotation of the Mersin ophiolite*

442

443 The early phase of rotation documented above is demonstrably of intraoceanic origin  
444 and associated with suprasubduction zone spreading of the Mersin ophiolite as it

445 occurs between two phases of dyke emplacement. In addition, rotation axes are  
446 broadly aligned with the restored trends of dykes in both the mantle sequence and  
447 metamorphic sole. Assuming that these are intruded perpendicular to the  
448 suprasubduction zone extension direction, this indicates rotation dominated by tilting  
449 around ridge-parallel axes.

450

451 In seafloor spreading systems, large rotations around shallowly plunging axes may  
452 be accommodated by normal faulting during plate divergence. For example, net  
453 tectonic rotation analyses in Troodos have highlighted rotations of dykes and lavas in  
454 the hanging wall of listric normal faults (Allerton and Vine, 1987; Hurst *et al.*, 1992)  
455 during the development of axial and off-axis graben structures by upper crustal  
456 extension. These faults dip symmetrically towards graben axes and are inferred to  
457 flatten at depth to sole out into detachments at the base of the upper crust (at the  
458 dyke-gabbro transition; Varga and Moores, 1985), without affecting deeper levels of  
459 the ophiolite. Large listric faults that dip towards the spreading axis have also been  
460 observed by seismic imaging in the slow-spreading Atlantic Ocean (e.g. Salisbury  
461 and Keen, 1993), but these sole out near the base of the crust. To accommodate the  
462 rotations observed in the Mersin ophiolite by listric faulting during spreading would,  
463 however, require faults that sole out at the base of the lithosphere (within the upper  
464 mantle). In addition, even if lithospheric-scale listric faults were capable of  
465 accommodating rotation of the Mersin crust and upper mantle, they would be  
466 incapable of capturing rocks of the metamorphic sole at depth (i.e. near their  
467 detachment level) and rotating these as well.

468

469 In contrast to downwards-convex listric faulting, displacement on upwards-convex  
470 oceanic detachment faults (Escartín and Canales, 2011) provides a viable potential  
471 mechanism for rotation of upper mantle, crustal and metamorphic sole rocks.  
472 Investigations of oceanic core complexes in the modern oceans (Garcés and Gee,  
473 2007; Morris *et al.*, 2009; MacLeod *et al.*, 2011) have shown that rolling hinge  
474 rotation of detachment fault footwalls around sub-horizontal, ridge-parallel axes is a  
475 characteristic signature of these lithospheric-scale structures. Within ophiolites,  
476 Maffione *et al.* (2013) showed that such fault systems may be recognised  
477 paleomagnetically using this characteristic rotation style. Most recently, Maffione *et*  
478 *al.* (2015) used a net tectonic rotation approach to document rotations around sub-  
479 horizontal axes of mantle-hosted intrusions in the lower Cretaceous suprasubduction  
480 zone ophiolites of south Tibet. Maffione *et al.* (2015) suggested that these rotations  
481 result from upper plate extension accommodated by widespread detachment faulting.  
482 They termed this process “forearc hyperextension” and inferred that structural  
483 dismemberment occurred shortly after magmatic accretion.

484

485 We propose that the early rotation documented in the Mersin ophiolite likewise is  
486 related to fore-arc (hyper)extension taken up by detachment-mode suprasubduction  
487 zone spreading. This is supported by four lines of argument: (i) rolling hinge rotations  
488 of the footwalls of oceanic detachment faults are characterized by ridge-parallel, sub-  
489 horizontal rotation axes (Garcés and Gee, 2007; Morris *et al.*, 2009; MacLeod *et al.*,  
490 2011), directly comparable to the style of rotation seen in Mersin (Fig. 6); (ii) rotation  
491 during the development of oceanic core complexes occurs very rapidly, as required  
492 by the full Mersin dataset based upon available age constraints. For example, along  
493 the Mid Atlantic Ridge, 46° of rotation of the Atlantis Massif footwall occurred in < 1.2

494 Myr (Morris *et al.*, 2009), whereas 64° of rotation of the 15°45'N oceanic complex  
495 was achieved within a very narrow inferred period of activity spanning a time interval  
496 between ~2.5 to 2.1 Ma (MacLeod *et al.*, 2011); (iii) oceanic detachment faults are  
497 lithospheric-scale structures that in the modern oceans have demonstrably exhumed  
498 mantle rocks onto the seafloor (Cannat *et al.*, 2006), and are therefore capable of  
499 rotating both crustal and mantle sections of the Mersin ophiolite around the same  
500 axis, in contrast to “standard” oceanic normal faults that only affect the brittle upper  
501 crust; and (iv) displacement on oceanic detachment faults tectonically juxtaposes  
502 rotated lower crustal and upper mantle rocks in their footwalls with unrotated upper  
503 crustal lavas in hanging wall blocks (MacLeod *et al.*, 2009), providing a plausible  
504 explanation for similar geological relationships in the Mersin and other Tauride  
505 ophiolites (where limited exposures of extrusive rocks are in close proximity to lower  
506 crustal/upper mantle rocks without an intervening sheeted dyke complex).

507

508 We note that the c. 82° early rotation seen in the Mersin ophiolite exceeds the range  
509 of footwall rotations observed in single oceanic detachment fault systems such as  
510 those sampled in the Atlantic Ocean (Fig. 6). However, numerical modeling of  
511 detachment faulting at slow-spreading ridges (Tucholke *et al.*, 2008) suggests that  
512 the active root zone of a weak, asymmetric fault should migrate with its hanging wall  
513 across the axis of rifting if magmatic accretion in the hanging wall takes up <<50% of  
514 the plate separation (Tucholke *et al.*, 2008; MacLeod *et al.*, 2009; Supplemental Fig.  
515 5). Reston and McDermott (2011) suggested that such migration would result in fault  
516 abandonment as a new fault cuts up from the rift axis through the preceding footwall  
517 (Supplemental Fig. 5), and invoked this mechanism to explain unroofing of broad  
518 expanses of mantle seen in the magma-poor rifted margins between Iberia and

519 Newfoundland. Capture of a portion of a previously rotated footwall section by a  
520 second, successor fault in this way can increase the net rotation experienced by the  
521 initial footwall, providing a mechanism capable of easily accommodating the  
522 magnitude of early rotation seen in the Mersin ophiolite.

523

## 524 *5.2 Mode of formation and rotation of the metamorphic sole*

525

526 The later, post-magmatic net rotation affecting the metamorphic sole of the Mersin  
527 ophiolite may have occurred: (i) in an intraoceanic, pre-obduction setting; (ii) during  
528 emplacement onto the Tauride margin; or (iii) have a composite origin. However, the  
529 consistency of rotation axes throughout the ophiolite is most simply explained by a  
530 common tectonic process related to spreading.

531

532 Dykes cutting the sole have geochemical signatures indicating derivation from partial  
533 melting of a depleted mantle wedge (Dilek *et al.*, 1999). Hence the metamorphic sole  
534 must have been above this melt source during dyke intrusion, requiring a mechanism  
535 for exhuming sole rocks from peak metamorphic depths to near the top of the mantle  
536 wedge. Models for the formation of metamorphic soles involving intraoceanic  
537 thrusting of young, hot oceanic lithosphere (e.g. Çelik, 2008) require dykes to intrude  
538 through the complete footwall of the under-thrust lithosphere in order to be emplaced  
539 into the metamorphic sole along the footwall-hanging wall contact. However, an  
540 alternative model involving formation of metamorphic soles along the upper interface  
541 of a down-going plate following subduction initiation and subsequent exhumation and  
542 welding of the sole rocks to the base of overriding plate has recently been proposed  
543 by van Hinsbergen *et al.* (2015). This model provides a mechanism for rapid

544 exhumation a newly-formed metamorphic sole to a position at the top of the mantle  
545 wedge, allowing post-metamorphic dyke intrusion through the sole very shortly after  
546 its formation. This is required in the case of the Tauride ophiolites, where ages of  
547 dykes and metamorphic sole rocks typically differ in age by < 3 Myr (Table 1; Parlak  
548 and Delaloye, 1996, 1999; Dilek *et al.*, 1999). The van Hinsbergen *et al.* (2015)  
549 model involves slab flattening in response to formation and extension of the  
550 suprasubduction zone crust, bringing sole rocks upwards to the base of the  
551 overriding lithosphere, followed by slab steepening in response to negative buoyancy  
552 resulting from eclogitization of the slab, leading to decoupling from the sole and influx  
553 of asthenosphere below the sole from which the intruding dykes derive.

554

555 This model provides a critical link between early rotation of the Mersin cumulates and  
556 mantle sequence dykes via fore-arc (hyper)extension involving oceanic detachment  
557 faulting and later rotation of dykes cutting the Mersin metamorphic sole. Welding of  
558 the metamorphic sole to the base of the mantle section via slab flattening would allow  
559 these rocks to be captured in the base of detachment fault footwall sections. This  
560 would allow rotation of the sole rocks around similar ridge-parallel, shallowly-plunging  
561 axes to those documented in the overlying ophiolite. As well as accounting for the  
562 similarity of rotation axes through the sampled units, this mechanism can also  
563 account for the rapid sequence of rotations required by our data, with all phases of  
564 rotation occurring over a restricted time interval of <~3 Myr during which crustal  
565 accretion, formation of the sole and dyke emplacement occurred.

566

567 *5.3 A conceptual model for rotation of an ophiolite and its metamorphic sole in a fore-*  
568 *arc environment*



569

570 Linking the upper plate process of fore-arc hyperextension (Maffione *et al.*, 2015)  
571 with the lower plate process of metamorphic sole formation and exhumation (van  
572 Hinsbergen *et al.*, 2015) leads to a combined conceptual model (Fig. 7) that can  
573 elegantly explain rapid, near-synchronous rotation of crust, mantle and sole around  
574 consistent ridge-parallel axes. This involves the following sequence of events:

575

576 a) initiation of an intraoceanic subduction zone, resulting concurrently in the early  
577 stages of formation of the future metamorphic sole (along the upper interface  
578 of the down-going plate) and suprasubduction zone spreading in the fore-arc  
579 region above the mantle wedge. This initial phase of magmatic spreading  
580 generates cumulate gabbros in the new suprasubduction zone lower crust and  
581 emplacement of dykes in the lithospheric mantle below (Fig. 7a);

582

583 b) amagmatic detachment-mode suprasubduction spreading, resulting in rotation  
584 of cumulate gabbros and mantle-hosted dykes in the footwall of an oceanic  
585 detachment fault (D1; Fig. 7b);

586

587 c) lack of melt supply leads to migration of the D1 detachment towards the locus  
588 of rifting (Tucholke *et al.*, 2008; Reston and McDermott, 2011; MacLeod *et al.*,  
589 2009), followed by initiation of a successor detachment (D2; Fig. 7c) that  
590 captures part of the rotated D1 footwall. Displacement on D2 then increases  
591 the rotation experienced by the cumulates and mantle-hosted dykes. At the  
592 same time, the down-going plate experiences slab flattening in response to  
593 suprasubduction zone spreading, mantle wedge volume decrease and upper

594 plate extension, leading to shallowing of the future metamorphic sole and  
595 development of its inverted pressure-temperature gradient (van Hinsbergen *et*  
596 *al.*, 2015);

597

598 d) at the plate contact, the metamorphic rocks at the top of the lower plate are  
599 welded to the base of the upper plate to form the metamorphic sole.

600 Eclogitization of the lower plate then results in negative buoyancy and the  
601 initiation of slab pull, resulting in decoupling from the sole and steepening of  
602 the slab. Influx of asthenospheric mantle into the wedge generates melt and  
603 leads to intrusion of dykes into the emplaced metamorphic sole (Fig. 7d); and

604

605 e) further displacement on the D2 detachment results in additional rotation of the  
606 cumulate gabbros and mantle-hosted dykes and in disruption of the  
607 metamorphic sole, part of which rotates in the D2 footwall (Fig. 7e).

608

## 609 **6. Conclusions**

610

611 Net tectonic rotation analysis of paleomagnetic data from the suprasubduction Mersin  
612 ophiolite reveals large rotations around shallowly-plunging rotation axes that are  
613 consistently oriented NE-SW, parallel to the inferred orientation of the Neotethyan  
614 spreading axis. The data are best explained by combining recent concepts of  
615 detachment-mode spreading (leading to fore-arc hyperextension; Maffione *et al.*,  
616 2015) and the formation and exhumation of metamorphic soles (van Hinsbergen *et*  
617 *al.*, 2015). Rotation of both the ophiolite and its metamorphic sole are inferred to be  
618 linked to rolling hinge rotation of detachment footwalls, as seen in oceanic core

619 complexes in modern (ultra-)slow spread lithosphere. This mode of spreading can  
620 also explain the absence of sheeted dyke complexes in several Upper Cretaceous  
621 Tauride ophiolites, as detachment-mode spreading characteristically results in  
622 tectonic juxtaposition of lower crustal and upper mantle rocks in detachment footwalls  
623 with upper crustal lavas in their hanging walls. Our results suggest that metamorphic  
624 sole rocks exhumed from peak metamorphic depths to the base of the  
625 suprasubduction zone lithosphere are then rotated as part of the upper plate. In  
626 addition, similar ages of crust and of dykes hosted in both the mantle and  
627 metamorphic sole require suprasubduction zone spreading, metamorphic sole  
628 exhumation, dyke emplacement and tectonic rotation to be essentially synchronous  
629 processes in a dynamic, intraoceanic fore-arc environment.

630

### 631 **Acknowledgements**

632 We thank the Ministry of Higher Education and Scientific Research (Iraq) for  
633 providing support for Ahmed Omer via a PhD scholarship held at Plymouth  
634 University. DJJvH acknowledges ERC Starting Grant 306810 (SINK) and NWO Vidi  
635 grant 864.11.004. Grateful thanks also to Osman Parlak for introducing us to the field  
636 geology of the Mersin ophiolite and for arranging field assistance by Çukurova  
637 University students during sampling. Net tectonic rotation analyses used the  
638 paleomagnetism.org application (Koymans *et al.*, 2016). Stereographic projections  
639 and Bingham statistics were produced using Richard Allmendinger's Stereonet  
640 program v. 9.9.4 (Cardozo *et al.*, 2013).

641

642

643

644 **References**

- 645 Allerton, S. and Vine, F. J., 1987. Spreading structure of the Troodos ophiolite,  
646 Cyprus: some palaeomagnetic constraints. *Geology*, **15**, 593-597.
- 647 Cannat, M., Sauter, D., Mendel, V., Ruellan, E., Okino, K., Escartín, J., Combier, V.  
648 and Baala, M., 2006. Modes of seafloor generation at a melt-poor ultraslow-  
649 spreading axis. *Geology*, **34**, 605-608, doi: 10.1130/G22486.1.
- 650 Cardozo, N. and Allmendinger, R. W., 2013, Spherical projections with  
651 OSXStereonet. *Computers & Geosciences*, **51**, 193 - 205, doi:  
652 10.1016/j.cageo.2012.07.021.
- 653 Çelik, Ö., 2008. Detailed Geochemistry and K-Ar Geochronology of the Metamorphic  
654 Sole Rocks and Their Mafic Dykes from the Mersin Ophiolite, Southern Turkey.  
655 *Turkish Journal of Earth Sciences*, **17**, 685-708.
- 656 Clube, T., Creer, K. and Robertson, A., 1985. Palaeorotation of the Troodos  
657 microplate, Cyprus, *Nature*, **317**, 522-525.
- 658 Deenen, M. H. L., Langereis, C. G., van Hinsbergen, D. J. J. and Biggin, A. J., 2011.  
659 Geomagnetic secular variation and the statistics of palaeomagnetic directions.  
660 *Geophysical Journal International*, **186**, 509-520.
- 661 Dilek, Y., Thy, P., Hacker, B. and Grundvig, S., 1999. Structure and petrology of  
662 Tauride ophiolites and mafic dike intrusions (Turkey): Implications for the Neotethyan  
663 ocean. *Geological Society of America Bulletin*, **111**, 1192.
- 664 Escartín, J. and Canales, J. P., 2011. Detachments in oceanic lithosphere:  
665 Deformation, magmatism, fluid flow, and ecosystems. *Eos Trans. AGU*, **92**, 31.

666 Garcés, M. and Gee, J. S., 2007. Paleomagnetic evidence of large footwall rotations  
667 associated with low- angle faults at the Mid- Atlantic Ridge. *Geology*, **35**, 279–282.

668 Gee, J. S. and Kent, D. V., 2007. Source of oceanic magnetic anomalies and the  
669 geomagnetic polarity time scale. *Treatise on Geophysics*, **5**, 455-507.

670 Granot, R., Abelson, M., Ron, H., Lusk, M. W. and Agnon, A., 2011. Direct evidence  
671 for dynamic magma supply fossilized in the lower oceanic crust of the Troodos  
672 ophiolite. *Geophysical Research Letters*, **38**, L16311, doi: 10.1029/2011GL048220.

673 Gurnis, M., Hall, C. and Lavier, L., 2004. Evolving force balance during incipient  
674 subduction. *Geochemistry, Geophysics, Geosystems*, **5**, Q07001, doi:  
675 10.1029/2003GC000681.

676 Hacker, B. R. and Gnos, E., 1997. The conundrum of Samail: explaining the  
677 metamorphic history. *Tectonophysics*, **279**, 215-226.

678 Hurst, S. D., Verosub, K. L. and Moores, E. M., 1992. Paleomagnetic constraints on  
679 the formation of the Solea graben, Troodos ophiolite, Cyprus. *Tectonophysics*, **208**,  
680 431–445, doi: 10.1016/0040-1951(92)90439-D.

681 Inwood, J., Morris, A., Anderson, M. W. and Robertson, A. H. F., 2009. Neotethyan  
682 intraoceanic microplate rotation and variations in spreading axis orientation:  
683 Palaeomagnetic evidence from the Hatay ophiolite (southern Turkey). *Earth and  
684 Planetary Science Letters*, **280**, 105-117.

685 Johnson, C.L., Constable, C. G., Tauxe, L., Barendregt, R., Brown, L. L., Coe, R. S.,  
686 Layer, P., Mejia, V., Opdyke, N. D., Singer, B. S., Staudigel, H. and Stone, D. B.,  
687 2008. Recent investigations of the 0–5 Ma geomagnetic field recorded by lava flows.  
688 *Geochemistry, Geophysics, Geosystems*, **9**, Q04032, doi: 10.1029/2007GC001696.

689 Koymans, M.R., Langereis, C.G., Pastor-Galan, D. and van Hinsbergen, D.J.J.,  
690 2016. Paleomagnetism.org: An online multi-platform open source environment for  
691 paleomagnetic data analysis. *Computers and Geosciences*, **93**, 127–137.

692 MacDonald, W. D., 1980. Net tectonic rotation, apparent rotation, and the structural  
693 tilt correction in palaeomagnetic studies. *Journal of Geophysical Research*, **85**, 3659-  
694 3669.

695 MacLeod, C., Allerton, S., Gass, I. and Xenophontos, C., 1990. Structure of a fossil  
696 ridge–transform intersection in the Troodos ophiolite. *Nature*, **348**, 717-720.

697 MacLeod, C. J., Searle, R. C., Murton, B. J., Casey, J. F., Mallows, C. Unsworth,  
698 S.C., Achenbach, K. L. and Harris, M., 2009. Life cycle of oceanic core complexes.  
699 *Earth and Planetary Science Letters*, **287**, 333-344, doi: 10.1016/j.epsl.2009.08.016..

700 MacLeod, C. J., Carlut, J., Escartín, J., Horen, H. and Morris, A., 2011. Quantitative  
701 constraint on footwall rotations at the 15°45'N oceanic core complex, Mid-Atlantic  
702 Ridge: implications for detachment fault processes. *Geochemistry, Geophysics,*  
703 *Geosystems*, **12**, Q0AG03, doi: 10.1029/2011GC003503.

704 MacLeod, C.J., Dick, H.J.B., Blum, P. and the Expedition 360 Scientists,  
705 2017. *Southwest Indian Ridge Lower Crust and Moho*. Proceedings of the  
706 International Ocean Discovery Program, 360: College Station, TX (International  
707 Ocean Discovery Program), doi: 10.14379/iodp.proc.360.2017.

708 Maffione, M., Morris, A. and Anderson, M. W., 2013. Recognizing detachment-mode  
709 spreading in the deep geological past. *Scientific Reports*, 3:2336, doi:  
710 10.1038/srep02336.

711 Maffione, M., van Hinsbergen, D. J. J., Koornneef, L. M. T., Guilmette, C., Hodges,  
712 K., Borneman, N., Huang, W., Ding, L., and Kapp, P., 2015. Forearc hyperextension  
713 dismembered the south Tibetan ophiolites. *Geology*, **43**, 475–478, doi:  
714 10.1130/G36472.1.

715 Maffione, M., van Hinsbergen, D., de Gelder, G., van der Goes, F. & Morris, A., 2017.  
716 Kinematics of Late Cretaceous subduction initiation in the Neo-Tethys Ocean  
717 reconstructed from ophiolites of Turkey, Cyprus, and Syria. *Journal of Geophysical*  
718 *Research: Solid Earth*, doi: 10.1002/2016JB013821

719 Morris, A. and Anderson, M. W., 2002, Palaeomagnetic results from the Baër-Bassit  
720 ophiolite of northern Syria and their implication for fold tests in sheeted dyke terrains.  
721 *Physics and Chemistry of the Earth*, **27**, 1215-1222.

722 Morris, A. and Maffione, M., 2016. Is the Troodos ophiolite (Cyprus) a complete,  
723 transform fault-bounded Neotethyan ridge segment?, *Geology*, **44**, 199–202,  
724 doi:10.1130/G37529.1.

725 Morris, A., Creer, K. M. and Robertson, A. H. F., 1990. Palaeomagnetic evidence for  
726 clockwise rotations related to dextral shear along the Southern Troodos Transform  
727 Fault, Cyprus. *Earth and Planetary Science Letters*, **99**, 250-262.

728 Morris, A., Anderson, M. W. and Robertson, A. H. F., 1998. Multiple tectonic rotations  
729 and transform tectonism in an intra-oceanic suture zone, SW Cyprus.  
730 *Tectonophysics*, **299**, 229-253.

731 Morris, A., Anderson, M. W., Robertson, A. H. F. and Al-Riyami, K., 2002. Extreme  
732 tectonic rotations within an eastern Mediterranean ophiolite (Baër -Bassit, Syria).  
733 *Earth and Planetary Science Letters*, **202**, 247–261, doi:10.1016/S0012-  
734 821X(02)00782-3.

735 Morris, A., Gee, J. S., Pressling, N., John, B. E., MacLeod, C. J., Grimes, C. B. and  
736 Searle, R. C., 2009. Footwall rotation in an oceanic core complex quantified using  
737 reorientated Integrated Ocean Drilling Program core samples. *Earth and Planetary*  
738 *Science Letters*, **287**, 217-228, doi: 10.1016/j.epsl.2009.08.007.

739 Parlak, O. and Delaloye, M., 1996. Geochemistry and timing of post metamorphic  
740 dyke emplacement in the Mersin Ophiolite (southern Turkey): New age constraints  
741 from  $^{40}\text{Ar}/^{39}\text{Ar}$  geochronology. *Terra Nova*, **8**, 585-592.

742 Parlak, O. and Delaloye, M., 1999. Precise  $^{40}\text{Ar}/^{39}\text{Ar}$  ages from the metamorphic  
743 sole of the Mersin ophiolite (southern Turkey). *Tectonophysics*, **301**, 145-158.

744 Parlak, O., Delaloye, M., and Bingöl, E., 1996a. Mineral chemistry of ultramafic and  
745 mafic cumulates as an indicator of the arc-related origin of the Mersin ophiolite  
746 (southern Turkey). *Geol. Rundsch.*, **85**, 647-661.

747 Parlak, O., Bozkurt, E. and Delaloye, M., 1996b. The obduction direction of the  
748 Mersin Ophiolite: structural evidence from subophiolitic metamorphics in the Central  
749 Tauride Belt, Southern Turkey. *International Geology Review*, **38**, 778-786.

750 Parlak, O., Karaoğlan, F., Rızaoğlu, T., Klötzli, U., Koller, F. and Billor, Z., 2013. U-  
751 Pb and  $^{40}\text{Ar}-^{39}\text{Ar}$  geochronology of the ophiolites and granitoids from the Tauride  
752 belt: Implications for the evolution of the Inner Tauride suture. *Journal of*  
753 *Geodynamics*, **65**, 22– 37.

754 Pearce, J. A. and Robinson, P. T., 2010. The Troodos ophiolitic complex probably  
755 formed in a subduction initiation, slab edge setting. *Gondwana Research*, **18**, 60-81,  
756 doi: 10.1016/j.ge.2009.12.003.



757 Petrovský, E. and Kapička, A., 2006. On determination of the Curie point from  
758 thermomagnetic curves. *Journal of Geophysical Research*, **111**, 1-10.

759 Reston, T. J. and McDermott, K. G., 2011. Successive detachment faults and mantle  
760 unroofing at magma-poor rifted margins. *Geology*, **39**, 1071-1074, doi:  
761 10.1130/G32428.1.

762 Robertson, A. H. F., 2002. Overview of the genesis and emplacement of Mesozoic  
763 ophiolites in the Eastern Mediterranean Tethyan region. *Lithos*, **65**,1-67.

764 Salisbury, M. H. and Keen, C. E., 1993. Listric faults imaged in oceanic crust.  
765 *Geology*, **21**, 117-120, doi: 10.1130/0091-7613(1993)021<0117:LFIIOC>2.3.CO;2.

766 Smith, D. K., Escartín, J., Schouten, H., Cann, J. R., 2008. Fault rotation and core  
767 complex formation: significant processes in seafloor formation at slow-spreading mid-  
768 ocean ridges (Mid-Atlantic Ridge, 13°–15°N). *Geochem. Geophys. Geosyst.*, **9**,  
769 Q03003. doi:10.1029/2007GC001699.

770 Staudigel, H., Gee, J. and Tauxe, L., 1992. Shallow intrusive directions of sheeted  
771 dikes in the Troodos ophiolite: Anisotropy of magnetic susceptibility and structural  
772 data. *Geology*, **20**, 841-844.

773 Stern, R. J. and Bloomer, S. H., 1992. Subduction zone infancy: Examples from the  
774 Eocene Izu-Bonin-Mariana and Jurassic California arcs. *Geol. Soc. Am. Bull.*, **104**,  
775 1621-1636.

776 Tekin, U. K., Bedi, Y., Okuyucu, C., Göncüoğlu, M. C. and Sayit, K., 2016.  
777 Radiolarian biochronology of upper Anisian to upper Ladinian (Middle Triassic)  
778 blocks and tectonic slices of volcano-sedimentary successions in the Mersin

779 Mélange, southern Turkey: New insights for the evolution of Neotethys. *Journal of*  
780 *African Earth Sciences*, **124**, 409-426, doi: 10.1016/j.jafrearsci.2016.09.039.

781 Torsvik, T. H., Van der Voo, R., Preeden, U., Mac Niocaill, C., Steinberger, B.,  
782 Doubrovine, P. V., van Hinsbergen, D. J., Domeier, M., Gaina, C. & Tohver, E., 2012.  
783 Phanerozoic polar wander, palaeogeography and dynamics. *Earth-Science Reviews*,  
784 **114**, 325–368, doi: 10.1016/j.earscirev.2012.06.002.

785 Tucholke, B. E., Behn, M. D., Buck, W. R. and Lin, J., 2008. Role of melt supply in  
786 oceanic detachment faulting and formation of megamullions. *Geology*, **36**, 455–458,  
787 doi:10.1130/G24639A.1.

788 van Hinsbergen, D. J. J., Peters, K., Maffione, M., Spakman, W., Guilmette, C.,  
789 Thieulot, C., Plümpner, O., Gürer, D., Brouwer, F. M., Aldanmaz, E. and Kaymakçı, N.,  
790 2015. Dynamics of intraoceanic subduction initiation: 2. Suprasubduction zone  
791 ophiolite formation and metamorphic sole exhumation in context of absolute plate  
792 motions. *Geochem. Geophys. Geosyst.*, **16**, doi:10.1002/2015GC005745.

793 van Hinsbergen, D. J. J., Maffione, M., Plunder, A., Kaymakçı, N., Ganerød, M.,  
794 Hendriks, B. W. H., Corfu, F., Gürer, D., de Gelder, G. I. N. O., Peters, K., McPhee,  
795 P. J., Brouwer, F. M., Advokaat, E. L. and Vissers, R. L. M., 2016. Tectonic evolution  
796 and paleogeography of the Kırşehir Block and the Central Anatolian Ophiolites,  
797 Turkey. *Tectonics*, **35**, 983-1014, doi: 10.1002/2015TC004018.

798 Varga, R. J. and Moores, E. M., 1985. Spreading structure of the Troodos ophiolite,  
799 Cyprus. *Geology*, **13**, 846-850, doi: 10.1130/0091-  
800 7613(1985)13<846:SSOTTO>2.0.CO;2.

801

802 **Figure captions**

803

804 Fig. 1. Summary of the geology of the Mersin ophiolite of southern Turkey. (a)  
805 Simplified geological map (after Tekin *et al.*, 2016); (b) tectonostratigraphic column  
806 (after Parlak *et al.*, 1996b). In this study we have sampled dykes cutting the  
807 metamorphic sole of the ophiolite, dykes cutting the mantle sequence, and ultramafic  
808 and gabbroic cumulates of the lower crust for paleomagnetic analysis.  
809 (a color version of this figure is available with the web version of the article).

810

811 Fig. 2. (a) Modal compositional layering in cumulate gabbros exposed along the  
812 Sorgun valley in the Mersin ophiolite (site MC09; compass-clinometer for scale). (b)  
813 Close-up of modal layering (coin for scale). In this example, compositional grading  
814 from olivine-rich bases to plagioclase-rich tops (X) combined with scour structures  
815 (dashed lines) provide way-up indicators that indicate overturning of the section.  
816 Darker area (Y) is a remnant of a thin (< 3 cm thick) basaltic dyke cutting the gabbros  
817 (sampled as site MC10).

818

819 Fig. 3. (a) High-temperature variations of low-field magnetic susceptibility ( $k$ ) showing  
820 maximum Curie temperatures of  $\sim 580^\circ\text{C}$ . Inset diagrams show the variation of  $1/k$ ,  
821 allowing accurate determination of Curie temperatures using the Petrovsky and  
822 Kapička (2006) method. (b) Isothermal remanent magnetization (IRM) acquisition  
823 curves showing presence of low coercivity magnetite.

824

825 Fig. 4. Typical examples of orthogonal demagnetization diagrams, showing well-  
826 defined, characteristic remanence directions isolated by both alternating field (AF)

827 and thermal (Th) treatment in all lithologies. Solid circles = horizontal plane; open  
828 symbols = vertical N-S or E-W plane.

829

830 Fig.5. Net tectonic rotation results from the Mersin ophiolite, combining site-level  
831 preferred solutions from each lithostratigraphic unit. (a) histograms of rotation angles;  
832 (b) contoured equal area stereographic projections of rotation axes; and (c) rose  
833 diagrams of restored initial dyke strikes. Note that rotation axes are consistently NE-  
834 SE-directed and parallel to initial dyke strikes. Inset diagrams show the results for  
835 early rotation of the dykes cutting the mantle section and for lower crustal cumulates  
836 found by back-stripping the mean net tectonic rotation determined from dykes in the  
837 metamorphic sole (representing the latest component of rotation in the Mersin  
838 ophiolite).

839 (a color version of this figure is available with the web version of the article).

840

841 Fig. 6. Equal area stereographic projections comparing (a) the style of the early  
842 rotation of the cumulate and mantle-hosted dykes of the Mersin ophiolite with footwall  
843 rotations documented in (b) the Atlantis Massif (Morris *et al.*, 2009) and (c) 15°45'N  
844 (MacLeod *et al.*, 2011) OCCs on the Mid Atlantic Ridge (MAR) and in (d) a fossil  
845 OCC preserved in the Mirdita ophiolite of Albania (Maffione *et al.*, 2013). The results  
846 for the Mersin ophiolite shown here represents an average amalgamating all net  
847 tectonic rotations solutions after back-stripping the effects of the later rotation of the  
848 metamorphic sole. Note that in all cases, rotation axes are shallowly-plunging and  
849 parallel to the observed or inferred orientation of the associated spreading axis.

850

851

852 Fig. 7. Conceptual model for rapid and extreme tectonic rotation of a  
853 suprasubduction zone ophiolite and its metamorphic sole in a fore-arc environment  
854 (see text for details). Note that detachment-mode spreading in the upper plate may  
855 involve development of multiple oceanic detachment faults, but the model shows only  
856 the minimum number of structures required to explain the Mersin paleomagnetic  
857 data.

858 (a color version of this figure is available with the web version of the article).

859

860 Table 1. Summary of geochronological constraints from the Mersin ophiolite.

861

862 Table 2. Paleomagnetic results from the Mersin ophiolite. Orientation of  
863 paleosurfaces (dyke margins; cumulate layering) are expressed as dip direction/dip.  
864 O/T = overturned. D, I, declination and inclination of *in situ* site mean remanence.  
865  $\Delta D$ ,  $\Delta I$ , declination and inclination error, respectively.  $k$ ,  $\alpha_{95}$ , precision parameter and  
866 95% cone of confidence around the site mean characteristic remanent  
867 magnetizations (ChRMs).  $K$ ,  $A_{95}$ , precision parameter and 95% cone of confidence  
868 around the site mean virtual geomagnetic pole (VGP).  $A_{95min}$ ,  $A_{95max}$ , minimum and  
869 maximum value of  $A_{95}$  expected from paleosecular variation of the geomagnetic field,  
870 according to Deenen et al. (2011).  $N$ , number of total samples used for the statistics.

871

872 Table 3. Net tectonic rotation parameters for dykes and cumulate rocks of the Mersin  
873 ophiolite

874

875 Supplemental Fig. 1. Equal area stereographic projections summarizing  
876 paleomagnetic results obtained from sites in the Mersin ophiolite. Blue circles =

877 specimen characteristic remanent magnetizations (ChRMs, top projections, with  
878 closed/open symbols indicating directions on the lower/upper hemispheres  
879 respectively) or corresponding virtual geomagnetic poles (VGPs, with mean rotated  
880 to vertical, bottom projections); green diamond = present day field direction  
881 (inclination = 56°); orange square = Late Cretaceous reference direction (inclination =  
882 40.2°); black circles = site mean magnetization directions; red circles =  $\alpha_{95}/A_{95}$  cones  
883 of confidence on site mean magnetizations/VGP distributions, respectively; dashed  
884 line = 45° cut-off on VGP distributions (following Johnson *et al.*, 2008). See Table 1  
885 for details of site locations and lithologies.

886

887 Supplemental Fig. 2. Illustration of the net tectonic rotation algorithm employed in this  
888 study, based on the Allerton and Vine (1987) method for (a) the paleovertical (dyke)  
889 case and (b) the paleohorizontal (layered gabbro) case. SMV = site magnetization  
890 vector (*in situ* remanence); RMV = reference magnetization vector; PDP = present  
891 day pole to paleosurface; IP = initial pole to paleosurface; RP = axis of net tectonic  
892 rotation; dotted line indicates circle of radius  $\beta$  (= angle between SMV and PDP)  
893 centred on RMV; dashed lines indicate great circles that bisect the pairs of vectors;  
894 subscripts 1 and 2 refer to alternative solutions in the dyke case, whereas the  
895 paleohorizontal case gives only one solution. Multiple application of this method for  
896 (c) the paleovertical and (d) paleohorizontal cases using all combinations of five  
897 estimates of SMV and PDP and three estimates of RMV. This yields 75 estimates of  
898 the rotation axis for each site, from which a mean estimate can be derived using  
899 Bingham statistics. Inset histograms illustrate the associated distributions of net  
900 tectonic rotation angles.

901

902 Supplemental Fig. 3. Net tectonic rotation results from individual dyke sites within the  
903 Mersin ophiolite. Results at each site are presented as a histogram of potential  
904 rotation angles, a contoured equal area stereographic projection of potential rotation  
905 axes and a rose diagram of restored initial dyke strikes.

906

907 Supplemental Fig. 4. Net tectonic rotation results from individual lower crustal  
908 cumulate sites within the Mersin ophiolite. Results at each site are presented as a  
909 histogram of potential rotation angles and a contoured equal area stereographic  
910 projection of potential rotation axes.

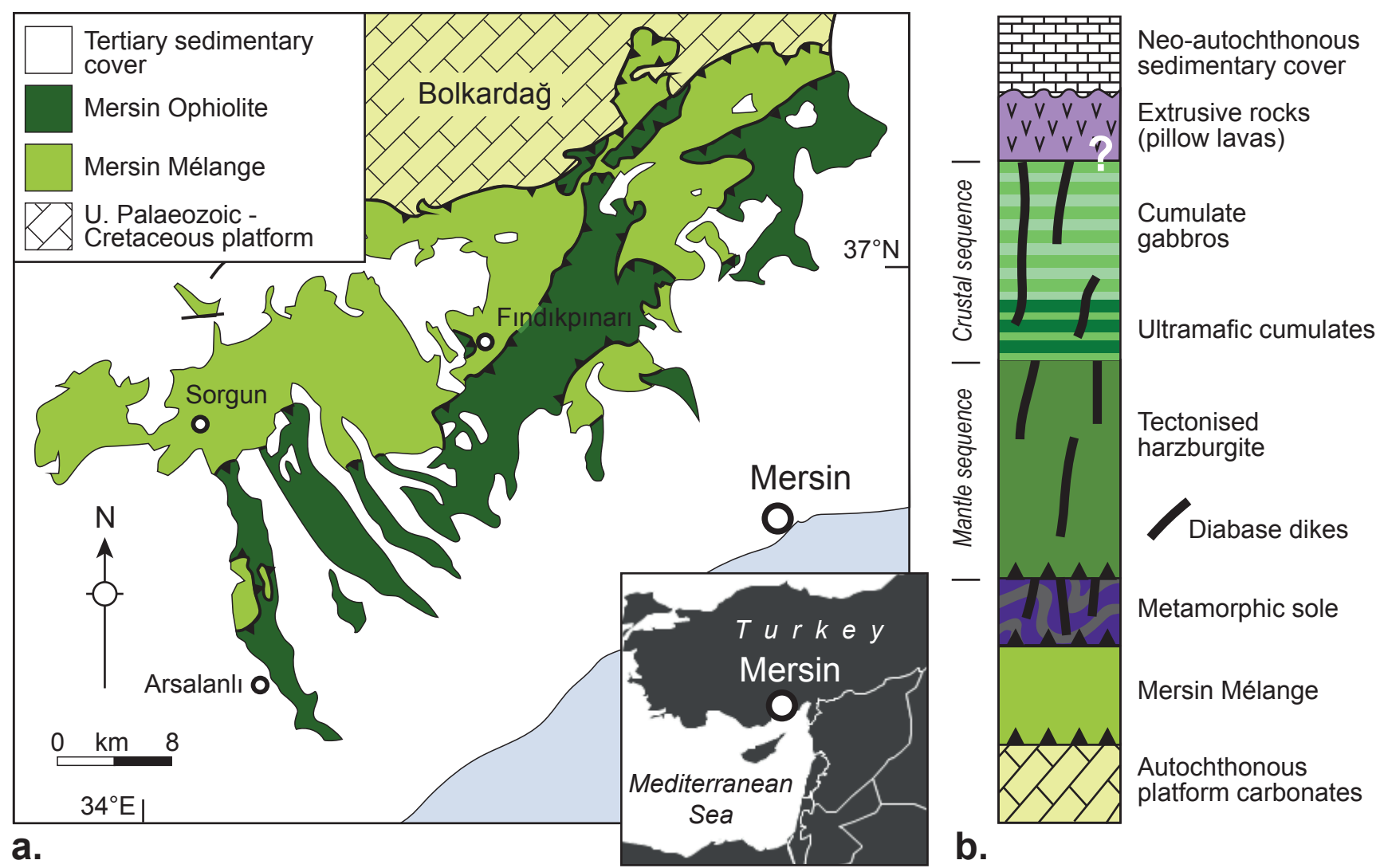
911

912 Supplemental Fig. 5. Accommodation of extreme rotation through displacement on  
913 successive oceanic detachment faults, based on the model of Reston and  
914 McDermott (2011). (a) Amagmatic extension is taken up on an oceanic detachment  
915 fault D1 rooted at the rift axis (grey arrow); (b) as the D1 footwall experiences rolling  
916 hinge rotation and is pulled out from beneath the hanging wall, the active fault root  
917 moves (white arrow) with the hanging wall over the rift axis; (c) the D1 detachment  
918 then becomes inactive and a new fault (D2) cuts up from the rift axis, capturing part  
919 of the rotated D1 footwall; (d) rolling hinge rotation of the D2 footwall increases the  
920 net rotation of the captured portion of the D1 footwall.

921

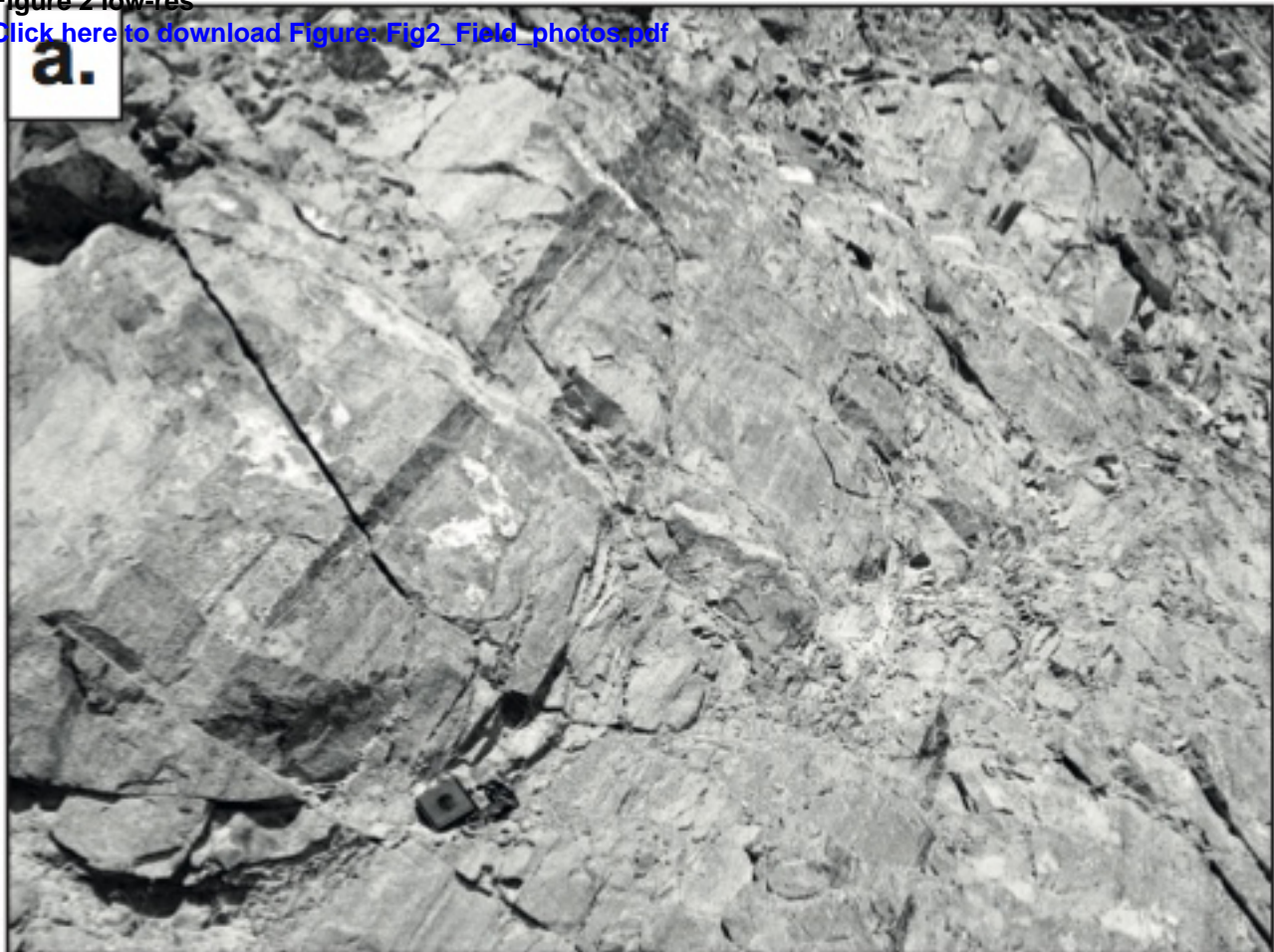
Figure 1 colour low-res

[Click here to download Figure: Fig1\\_Map\\_colour.pdf](#)





**a.**



**b.**



Figure 3 low-res

[Click here to download Figure: Fig3\\_Rock\\_magnetism.pdf](#)

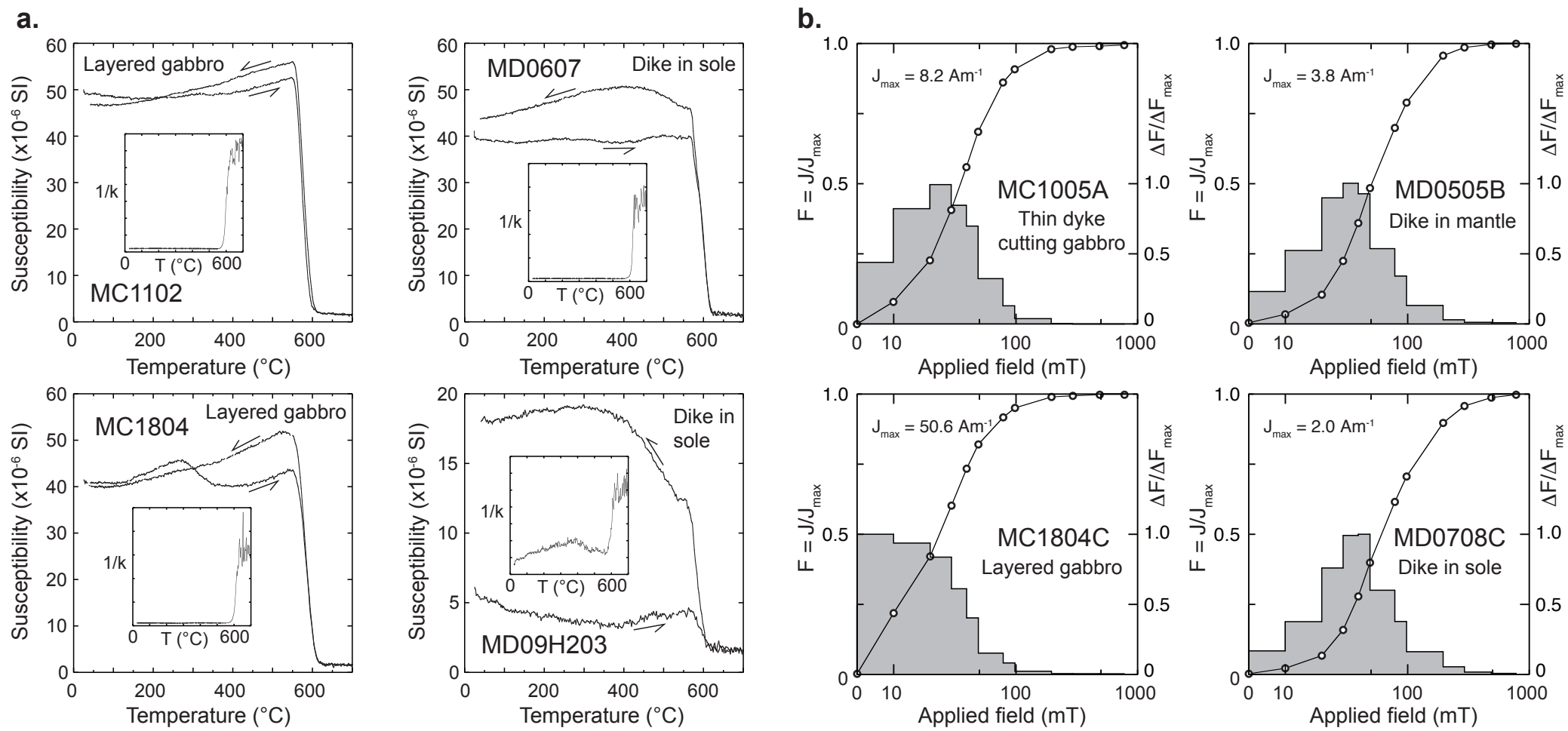
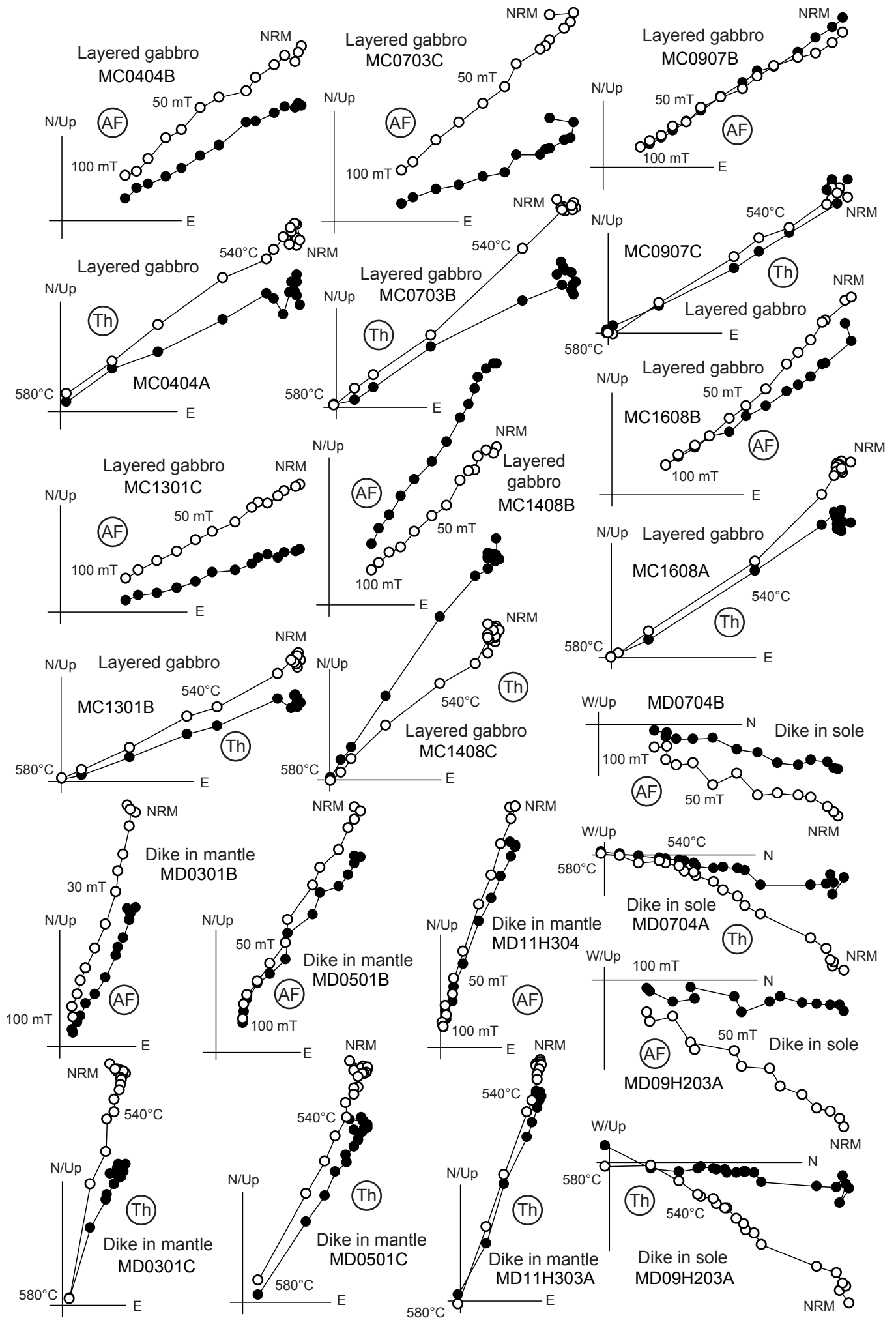


Figure 4 low-res  
[Click here to download Figure: Fig4\\_Z-plots.pdf](#)



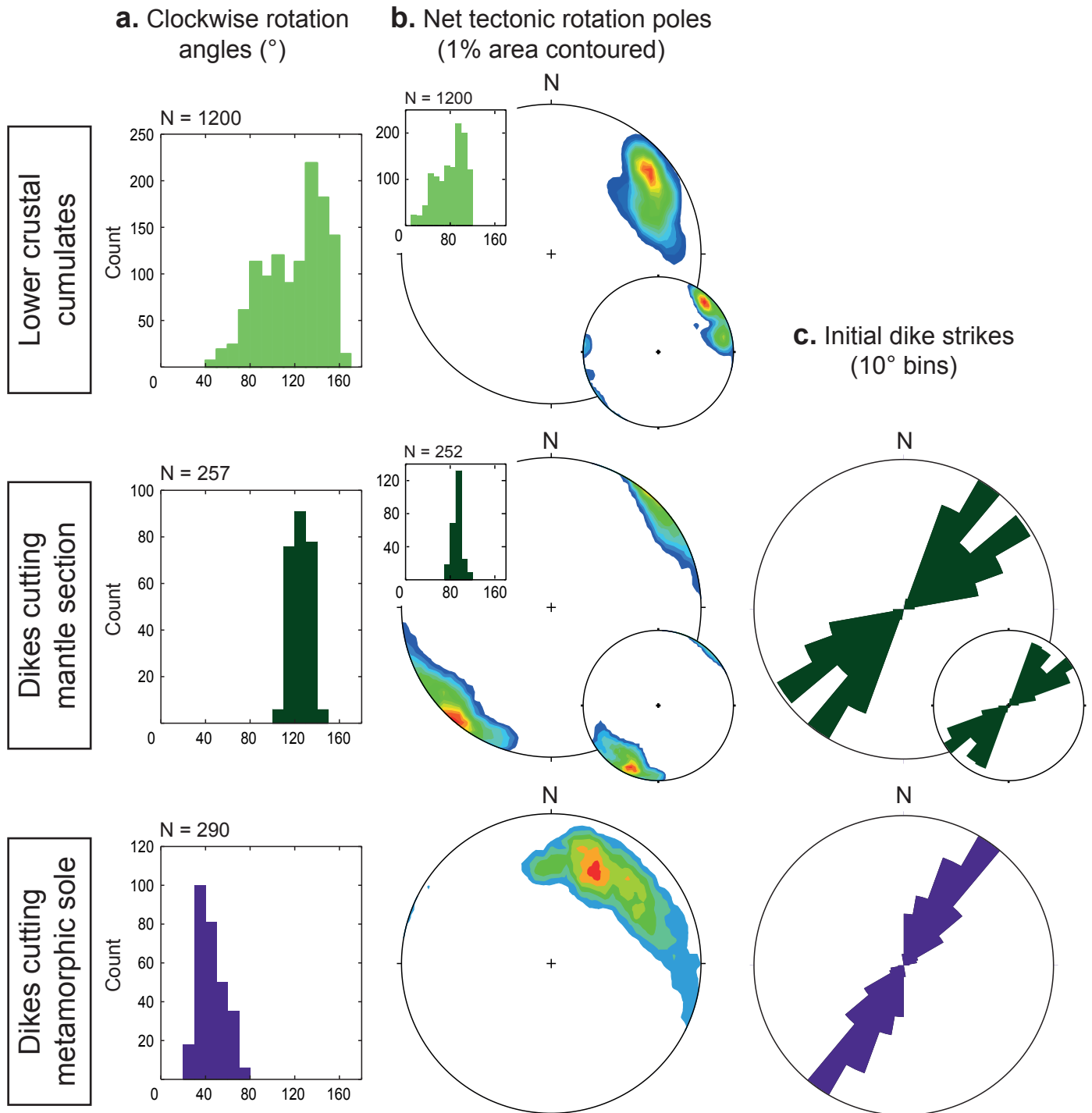


Figure 6 low-res

[Click here to download Figure: Fig6\\_OCC\\_comparison.pdf](#)

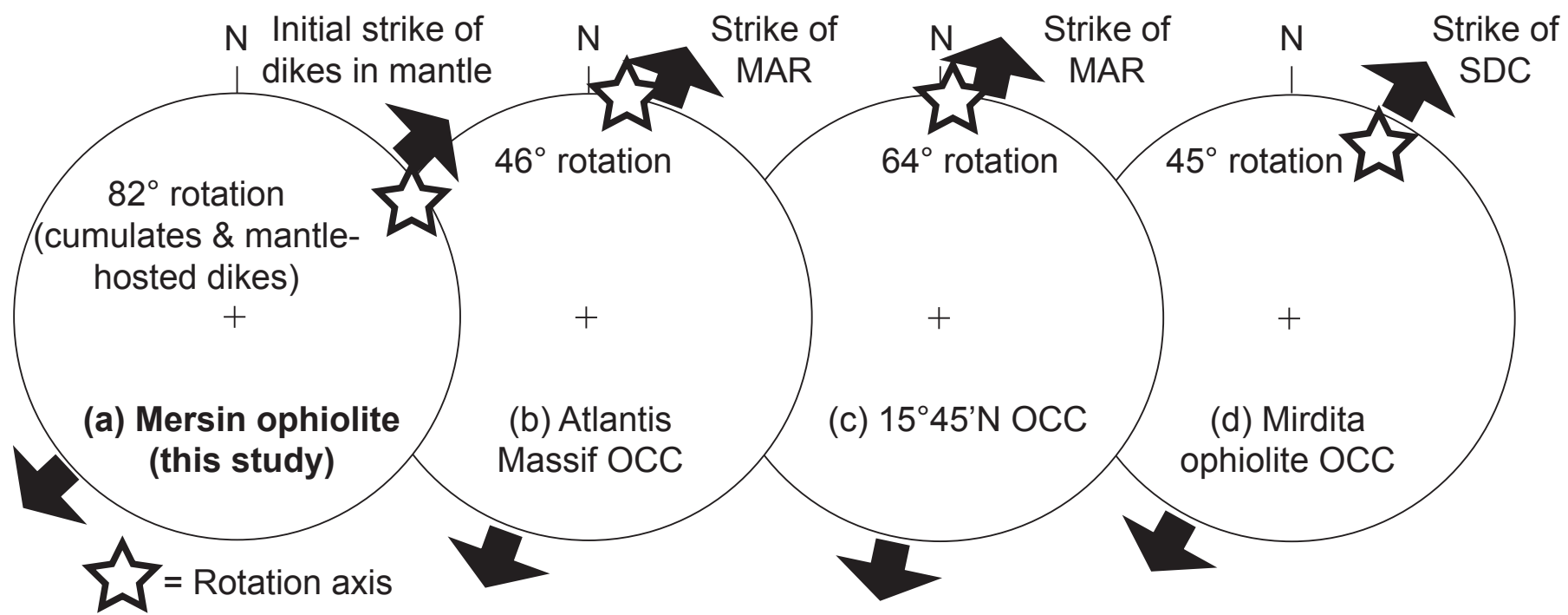


Figure 7 colour low-res

[Click here to download Figure: Fig7\\_Final\\_model\\_colour.pdf](#)

